Possibilities of warm cloud microstructure profiling with multiple-field-of-view Raman lidar

Aleksey V. Malinka* and Eleonora P. Zege

B. I. Stepanov Institute of Physics, National Academy of Science of Belarus, Pr. Nezavisimosti 68, Minsk 220072, Belarus

*Corresponding author: mal@light.basnet.by

Received 6 August 2007; revised 15 October 2007; accepted 23 October 2007;
posted 23 October 2007 (Doc. ID 86187); published 3 December 2007

The possibilities of cloud characteristics retrieval with multiple-field-of-view Raman lidar are considered. It has been shown that the Raman lidar return is sensitive to two cloud characteristics; the scattering coefficient and the effective droplet size. This sensitivity is studied and the optimal receiver fields-of-view (FOVs) for cloud sounding are recommended. The optimal FOV values are estimated to be approximately R/H (R, the collecting optics radius, H, the cloud altitude) to measure the scattering coefficient profiles, and $\sim 0.01z/H$ for the droplet size measurements (z, the cloud thickness). The algorithm based on the iterative scheme and singular value decomposition as a regularization procedure is presented and verified using computer simulation. The recommendations for profile retrieval with variable altitude resolution are given.

OCIS codes: 280.3640, 290.4210.

1. Introduction

Cloud profiling provides important information for radiation budget and climate change investigation [1]. Warm (water-droplet) clouds are an important factor in the indirect aerosol effect on climate and play a key role in weather forming [2,3]. The main instruments of warm cloud profiling are radars and lidars. They are complementary. Radars fail to retrieve the cloud bottom characteristics because of virga (drizzle falling below cloud base, not the cloud droplets completely defines the radar signal due to its Rayleigh type of size dependence of power 6). Lidars do not provide the cloud characteristics at large depths, because of strong signal attenuation but are advisable for sounding the near-bottom range of clouds (within several hundred meters) [4–7]. Therefore, the synergy of only these two techniques is able to provide the appropriate cloud profiling, because the lidar retrieval of cloud characteristics in the near-bottom range is necessary as a starting point for algorithms of radar cloud profiling.

It was shown in [8] that practically the only two characteristics of a warm cloud that could be retrieved from lidar sounding are the scattering coefficient σ and the effective particle radius r_{32}. The effective particle radius is the area weighted mean radius. The other parameters of the droplet size distribution have negligible effect on lidar signals. Some important cloud characteristics, such as the number or volume concentration of droplets, can be given in terms of these two (σ and r_{32}).

Raman lidar sounding with a narrow field of view (FOV) is a common way to measure profiles of the extinction coefficient [9,10]. The idea to measure the effective particle radius with the multiple-field-of-view (MFOV) elastic lidar (with the use of multiple scattering returns) was put forward [11] and successfully realized [12–14]. However, the retrieval of particle radius from MFOV elastic lidar measurements is complicated by nonmonotonic sophisticated behavior of droplet phase functions in the vicinity of the backward direction [15,16]. On the other hand, as it was shown in [17], this drawback could be overcome with a MFOV Raman lidar. In this case all features of the elastic multiple scattering are kept, but the phase function in near-backward direction can be considered as isotropic for Raman scattering [18,19].

The objectives of this paper are to specify the optimal FOVs that provide the maximal sensitivity of the registered signals to the scattering coefficient and the

0003-6935/07/358419-09$15.00/0

effective particle radius, to develop the retrieval procedure, and to study the retrieval capabilities of MFOV Raman lidar.

2. Technique to Simulate a MFOV Raman Lidar Return from a Stratified Cloud

The main feature of MFOV lidar sounding of clouds is that the multiple scattering contributes predominantly to the signals at some FOVs. To describe a Raman lidar return with multiple scattering we use the model presented in [19]. According to this model, the power F of the Raman lidar return as a function of receiver FOV γ_r and sounding depth z,

$$z = \frac{ct}{2} - H, \tag{1}$$

c is the speed of light, t is the photon arrival time, H is the altitude of the cloud base, is given by

$$F(\gamma_r,\ z) = C_{\max}\int \frac{\nu d\nu}{2\pi}\ \varphi_{eff}(\nu)\exp\Bigg(-\int_0^z \big[\varepsilon_{eff}(\xi) - \sigma_{eff}(\xi)P_{eff}^{\ f}(\xi,\ \nu(z-\xi))\big]d\xi\Bigg), \tag{2}$$

where $C_{\max}$ is a calibration constant that specifies the maximum number of photocounts, corresponding to the altitude H just below the cloud. The function $\varphi_{eff}(\nu)$ is the Fourier transform of the source-receiver effective diagram. In the case of a monostatic coaxial system with a circular homogeneous source and receiver diagrams this function is defined as

$$\varphi_{eff}(\nu) = \frac{1}{(z+H)^2}\ \frac{2J_1(\nu R_s)}{\nu R_s}\ \frac{2J_1[\nu(z+H)\gamma_s]}{\nu\gamma_s} \times \frac{2\pi R_r J_1(\nu R_r)}{\nu}\ \frac{2\pi\gamma_r J_1[\nu(z+H)\gamma_r]}{\nu}, \tag{3}$$

where R_s and R_r are the source (beam) and receiver (primary mirror/lens) radii, respectively, γ_s and γ_r are the source beam divergence and the receiver FOV (both of them are half-angles throughout the paper), $J_k(x)$ is the Bessel function of the kth order, $\varepsilon_{eff}(z)$ and $\sigma_{eff}(z)$ are effective extinction and scattering coefficients, which are equal to

$$\varepsilon_{eff}(z) = \varepsilon(\lambda_0,\ z) + \varepsilon(\lambda_R,\ z),$$
$$\sigma_{eff}(z) = \sigma(\lambda_0,\ z) + \sigma(\lambda_R,\ z), \tag{4}$$

where λ_0 and λ_R are the initial and Raman-shifted wavelengths, respectively, $P_{eff}^{\ f}(p)$ is the Hankel transform (p is the angular frequency),

$$P_{eff}^{\ f}(p) = \frac{1}{2}\int_0^\infty P_{eff}^{\ f}(\theta)J_0(p\theta)\theta d\theta, \tag{5}$$

of the effective forward scattering phase function:

$$P_{eff}^{\ f}(z,\ \theta) = \frac{\sigma(\lambda_0,\ z)P^f(\lambda_0,\ z,\ \theta) + \sigma(\lambda_R,\ z)P^f(\lambda_R,\ z,\ \theta)}{\sigma(\lambda_0,\ z) + \sigma(\lambda_R,\ z)}. \tag{6}$$

Here $P^f(\lambda, z, \theta)$ is the forward scattering phase function defined within the small-angle approximation [20] for elastic scattering at wavelength λ.

For clouds the extinction coefficient in the visible is equal to the scattering one and it does not depend on wavelength:

$$\varepsilon(\lambda_0,\ z) = \varepsilon(\lambda_R,\ z) = \sigma(\lambda_0,\ z) = \sigma(\lambda_R,\ z) = \sigma(z). \tag{7}$$

It is shown in [8] that the effective forward scattering phase function (6) of warm clouds depends in fact on one cloud parameter only, namely, on the effective dimensionless droplet radius ρ:

$$\rho(z) = \pi r_{32}(z)\left(\frac{1}{\lambda_0} + \frac{1}{\lambda_R}\right). \tag{8}$$

Thus, the depth dependence appears in the form:

$$P_{eff}^{\ f}(z,\ \theta) = P^f(\rho(z),\ \theta), \tag{9}$$

$$P_{eff}^{\ f}(z,\ p) = P^f(\rho(z),\ p). \tag{10}$$

Therefore, Eq. (2) becomes

$$F(\gamma_r,\ z) = C_{\max}\int \frac{\nu d\nu}{2\pi}\ \varphi_{eff}(\nu)\exp\Bigg(-2\int_0^z \sigma(\xi) \times \big[1 - P^f(\rho(\xi),\ \nu(z-\xi))\big]d\xi\Bigg). \tag{11}$$

To provide a fast code for the simulation of Raman lidar returns we use the approximation in which the forward scattering phase function of clouds is represented as the sum of Fraunhofer diffraction and a geometrical optics component [21]:

$$P(\rho,\ \theta) = \frac{1}{2}\big(\rho^2 P^D(\rho\theta) + P^{GO}(\theta)\big). \tag{12}$$

[Note, that only the first term of Eq. (12) depends on droplet size.] The geometrical optics component P^{GO} is calculated by Fresnel formulas including the light reflected and once refracted by a droplet with the refractive index of 1.33 [22]. This component practically does not depend on the wavelength and drop sizes. The diffraction part $\rho^2 P^D(\rho\theta)$ is calculated for the Cloud C.1-like model (gamma distribution) [23]:

$$\frac{dp}{dr} = \frac{r^\mu}{\mu!}\left(\frac{r_{32}}{\mu+3}\right)^{-\mu-1}\exp\left(-\frac{\mu+3}{r_{32}}\ r\right), \tag{13}$$

where r is a droplet radius, dp is a probability that the droplet radius is in the interval from r to $r + dr$, μ is a gamma-distribution parameter taken equal to 6.

In the Fourier space Eq. (12) becomes

$$P(\rho, p) = \frac{1}{2}\left(P^D(p/\rho) + P^{GO}(p)\right). \tag{14}$$

A stratified cloud is considered as consisting of N layers, each layer i being characterized by two parameters: σ_i and ρ_i.

Then Eq. (11) becomes

$$F(\gamma_r, z) = C_{\max}\int \frac{\nu d\nu}{2\pi}\,\varphi_{eff}(\nu)\exp\left(-2\tau + \sum_{i=1}^{N}\sigma_i\int_{z_{i-1}}^{z_i}\left[P^D\left(\frac{z-\xi}{\rho_i}\,\nu\right) + P^{GO}((z-\xi)\nu)\right]d\xi\right), \tag{15}$$

where τ is the optical depth. In Eq. (15) we formally put

$$P^D(p<0) = P^{GO}(p<0) \equiv 0. \tag{16}$$

Equation (15) can be rewritten in the form

$$F(\gamma_r, z) = C_{\max}\int \frac{\nu d\nu}{2\pi}\,\varphi_{eff}(\nu)\exp(-2\tau)G^D G^{GO}, \tag{17}$$

where

$$G^D = \exp\left(-\sum_{i=1}^{N}\frac{\sigma_i\rho_i}{\nu}\left[R^D\left(\frac{\Delta z_i}{\rho_i}\,\nu\right) - R^D\left(\frac{\Delta z_{i-1}}{\rho_i}\,\nu\right)\right]\right),$$

$$G^{GO} = \exp\left(-\sum_{i=1}^{N}\frac{\sigma_i}{\nu}\left[R^{GO}(\Delta z_i\nu) - R^{GO}(\Delta z_{i-1}\nu)\right]\right), \tag{18}$$

with

$$R^D(p) = \int_0^p P^D(x)dx, \qquad R^D(p<0) \equiv 0,$$

$$R^{GO}(p) = \int_0^p P^{GO}(x)dx, \qquad R^{GO}(p<0) \equiv 0, \tag{19}$$

$$\Delta z_i = z - z_i, \tag{20}$$

i is the layer number, z_i is the depth of the layer border.

The equations presented in this section constitute the algorithm for very fast computer simulation of the Raman lidar return from stratified clouds with multiple scattering.

3. Lidar Return Sensitivity to the Cloud Characteristics

We define the sensitivity $C_i^{\rho}(\gamma_r, z)$ of the signal $F(\gamma_r, z)$ to the particle radius in the ith layer as a logarithmic derivative:

$$C_i^{\rho}(\gamma_r, z) = \frac{\rho_i}{F(\gamma_r, z)}\,\frac{\partial F(\gamma_r, z)}{\partial \rho_i}. \tag{21}$$

According to Eqs. (17) and (18), it is equal to

$$C_i^{\rho}(\gamma_r, z) = \frac{C_{\max}}{F(\gamma_r, z)}\int \frac{\nu d\nu}{2\pi}\,\varphi_{eff}(\nu)\exp(-2\tau)\rho_i\,\frac{\partial G^D}{\partial \rho_i}\,G^{GO}, \tag{22}$$

where

$$\frac{\rho_i}{G^D}\,\frac{\partial G^D}{\partial \rho_i} = -\frac{\sigma_i\rho_i}{\nu}\left[R^D\left(\frac{\Delta z_i}{\rho_i}\,\nu\right) - R^D\left(\frac{\Delta z_{i-1}}{\rho_i}\,\nu\right)\right] + \sigma_i\left[\Delta z_i P^D\left(\frac{\Delta z_i}{\rho_i}\,\nu\right) - \Delta z_{i-1}P^D\left(\frac{\Delta z_{i-1}}{\rho_i}\,\nu\right)\right]. \tag{23}$$

A similar definition is used for the signal sensitivity to the value of σ_i in the ith layer:

$$C_i^{\sigma}(\gamma_r, z) = \frac{\sigma_i}{F(\gamma_r, z)}\,\frac{\partial F(\gamma_r, z)}{\partial \sigma_i}. \tag{24}$$

From Eqs. (17) and (18) we get

$$C_i^{\sigma}(\gamma_r, z) = \frac{C_{\max}}{F(\gamma_r, z)}\int \frac{\nu d\nu}{2\pi}\,\varphi_{eff}(\nu)\sigma_i D, \tag{25}$$

where

$$D = -2(z_i - z_{i-1}) - \frac{\rho_i}{\nu}\left[R^D\left(\frac{\Delta z_i}{\rho_i}\,\nu\right) - R^D\left(\frac{\Delta z_{i-1}}{\rho_i}\,\nu\right)\right] - \frac{1}{\nu}\left[R^{GO}(\Delta z_i\nu) - R^{GO}(\Delta z_{i-1}\nu)\right]\left[\exp(-2\tau)G^D G^{GO}\right]. \tag{26}$$

Figure 1 gives examples of the calculation of the function $C_i^{\rho}(\gamma_r, z)$ for the cases of two-layered and ten-layered clouds. There are several clear observations to be extracted from Fig. 1.

1. The sensitivity level is high enough to make size retrieval possible.

2. The sensitivity to drop size in ith layer increases when z is approaching the far end of this layer, having the maximum just behind this layer, and then it goes down, however, not very fast.

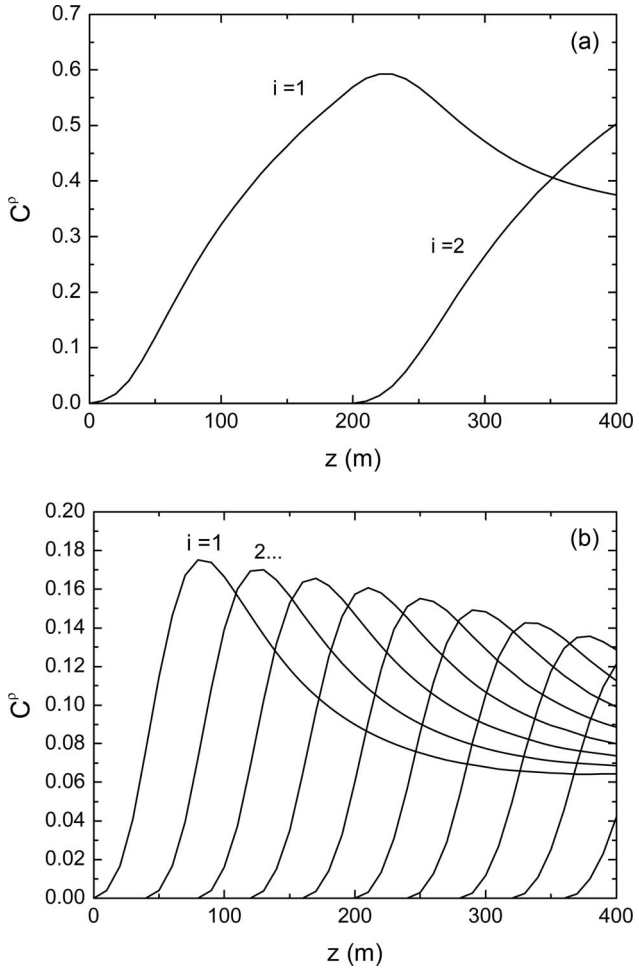

Fig. 1. Sensitivity of the signal to drop size in the ith layer: (a) two-layered cloud and (b) ten-layered cloud. The cloud altitude is 2000 m, the cloud thickness is 400 m, the source divergence and the receiver FOV are 0.05 and 0.5 mrad, respectively, the source and receiver radii are 0.1 and 0.5 m, respectively, the scattering coefficient is 0.01 m^{-1}, $\rho = 100$.

3. The sensitivity of the signal to the drop size in the layer, located ahead of the depth from which the signal originates has a significant value. Vice versa, for the layer located behind this depth it is strictly equal to zero. The reason for such behavior is obvious. The photon coming from depth z could not be scattered within the layer located deeper than depth z, however it "remembers" the history of scattering within the layers located before z.

4. The sensitivity decreases with the number of layers. This point is also evident, because the thinner the layer, the less the number of multiple scattering events occurring in it. However this point is of great importance, because it determines the problem: what is the tradeoff between the desired altitude resolution of the profile retrieval and the retrieval error, e.g., can we estimate only some effective droplet size for the entire cloud, or can we altitude-resolve its profile with reasonable accuracy? This point will be addressed below in detail.

4. Optimization of Lidar System

To optimize the lidar system we need to specify the FOVs at which the signal is most sensitive to the scattering coefficient and the droplet size. Let us start with considering the homogeneous cloud layer. The optimal FOV for measuring the scattering coefficient is easy to find. It is the FOV that maximizes the single scattering contribution.

In Fig. 2(a) the single scattering, multiple scattering, and total signals are plotted versus FOV. Note, that Fig. 2(a) presents the signal integrated over FOV rather than the angular distribution of the signal in the receiver plane. The vertical lines correspond to the values of

$$\gamma_1 = \max\left\{\gamma_s, \frac{R_r}{z+H}, \frac{R_s}{z+H}\right\}, \tag{27}$$

$$\gamma_2 = \gamma_s + \frac{R_r}{z+H} + \frac{R_s}{z+H}. \tag{28}$$

The value γ_2 corresponds to full overlap of the source and receiver diagrams (there is no single scattering

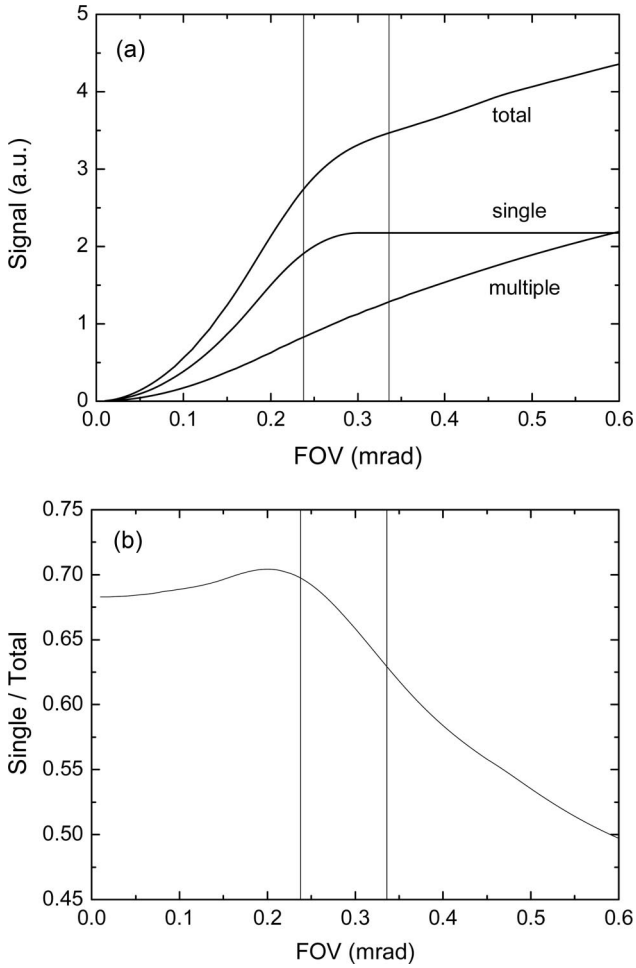

Fig. 2. (a) Single scattering, multiple scattering, and total signal and (b) relative contribution of single scattering versus FOV. Vertical lines, the values of γ_1 and γ_2; sounding depth $z = 100$; other parameters are the same as in Fig. 1.

outside this cone), hence, the FOV to measure single scattering should not exceed this value. As seen from Fig. 2(b), the maximum single scattering contribution is near the first value γ_1 (even less). However, whereas the signal increases rapidly with FOV until the value of γ_1, we would recommend to set the value of the FOV between γ_1 and γ_2, but closer to γ_1, for the extinction measurement, because the signal energy is always crucial for Raman lidar sounding. The value $R_r/(z + H)$ is usually greater that the other values in Eq. (27), so the value R_r/H is close to γ_1 and always satisfies the inequality

$$\gamma_1 < R_r/H < \gamma_2. \tag{29}$$

Thus, the value R_r/H is the estimation of the optimal FOV for extinction measurement. For instance, for a telescope radius of 0.5 m and a cloud altitude of 2 km, it equals 0.25 mrad. In general, the greater value of $(R_r/H, \gamma_s)$ should be taken.

In Fig. 3(a) the sensitivity C^σ is plotted for FOV for different optical depths (from 1 to 4). It is seen that the above-mentioned interval (shown with vertical lines) overestimates a bit the FOV value of maximal sensitivity. However, the sensitivity in this interval does not differ a lot from its maximal value, and, on the other hand, the signal energy in this interval is much greater than it could be with smaller FOV.

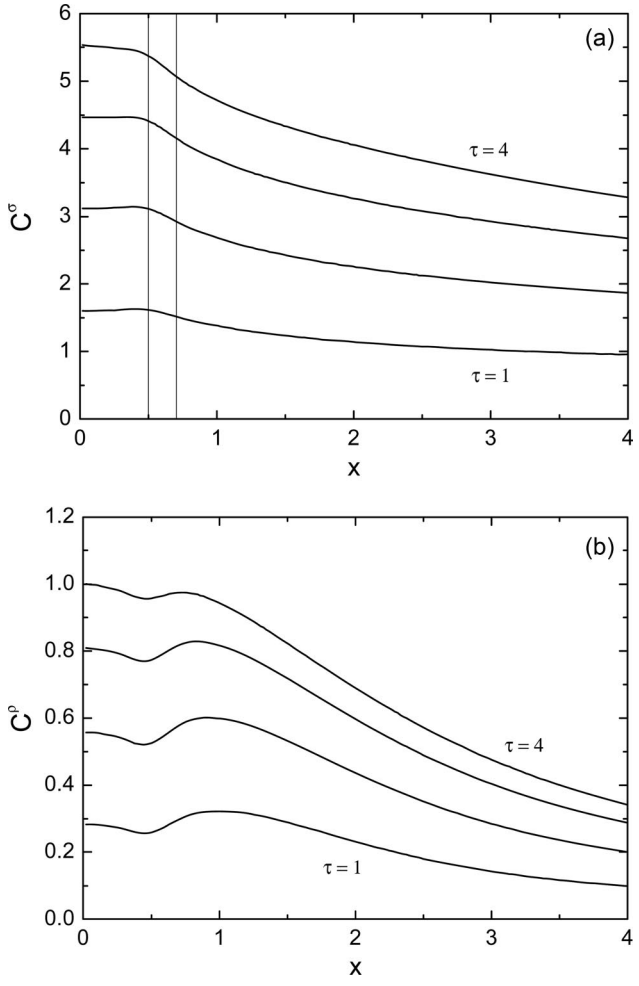

Fig. 3. Signal sensitivity to the (a) extinction coefficient and to the (b) drop size. The abscissa is defined with Eq. (30). The optical depths are equal to 1, 2, 3, and 4.

In Fig. 3(b) there is the sensitivity to particle radius C^ρ for different depths. The abscissa variable x is

$$x = \frac{\rho\gamma_r(z + H)}{z}, \tag{30}$$

which is the only variable that involves the FOV value within the small angle and the Fraunhofer diffraction approximations. It is seen that the maximal sensitivity is about the point $x = 1$ at different optical depths (1–4). The calculation was made for the effective particle radius of 9 μm. In this case the sensitivity maximum occurs at a FOV of ~1 mrad. For other values of the effective radius this maximum shifts. Cloud droplet radii mainly range from 4 to 20 μm, therefore the FOV providing the maximum changes from 0.5 to 2 mrad. However, whereas the sensitivity as a function of FOV is smooth enough in the vicinity of its maximum and the shift of this maximum for various cloud microstructures is moderate, the optimal FOV defined for a drop size of 9 μm (or $\rho = 100$ for 532 nm initial wavelength) may be used for warm cloud microstructure profiling. With $H \gg z$, $\rho = 100$, and the maximum position $x = 1$ from Eq. (30) we get

$$\gamma_r \approx 0.01z/H. \tag{31}$$

This is the FOV value we could recommend for measuring the droplet size.

5. Inversion Scheme

In this section we propose the algorithm to retrieve the scattering coefficient and the effective dimensionless droplet radius of a warm cloud. We consider the cloud as consisting of N layers, each with its own characteristics. These unknown characteristics comprise a $2N$ length vector (σ_i, ρ_i), where $i = 1{:}N$. As lidars have usually no absolute calibration, we add the calibration constant $C_{\max}$ as an additional unknown variable. That is, the sought value is the $2N + 1$ length vector

$$\mathbf{X} = (\sigma_i,\ \rho_i,\ C_{\max}). \tag{32}$$

As primary data we consider the two depth-dependent signals, measured with two FOVs, defined above:

$$\mathbf{F}^m = \left[F^m(\gamma_1,\ z_n),\ F^m(\gamma_2,\ z_n)\right]. \tag{33}$$

This vector is considered as a function of $\mathbf{X}$:

$$\mathbf{F}^m = \mathbf{F}(\mathbf{X}). \tag{34}$$

To solve Eq. (34) we use an iterative scheme. The initial value of $\mathbf{X}$ is chosen as follows: the droplet radius is set equal to 9 μm throughout the cloud, and σ_i and $C_{\max}$ are calculated from the signal at the smallest FOV $F^m(\gamma_1, z_n)$ within the framework of the single scattering approximation.

Then the correction to $\mathbf{X}$ is found by solving the equation [see, e.g., 24]

$$\frac{\Delta \mathbf{F}}{\mathbf{F}} = \frac{\Delta \mathbf{X}}{\mathbf{X}} \mathbf{C}, \tag{35}$$

where $\mathbf{C}$ is the matrix of the logarithmic derivatives of the function $\mathbf{F}(\mathbf{X})$ from Eq. (34):

$$\mathbf{C}_{in} = \begin{bmatrix} C_i^{\sigma}(\gamma_1, z_n) & C_i^{\sigma}(\gamma_2, z_n) \\ C_i^{\rho}(\gamma_1, z_n) & C_i^{\rho}(\gamma_2, z_n) \\ 1 & 1 \end{bmatrix}, \tag{36}$$

(the last row is the logarithmic derivative of $\mathbf{F}$ with respect to $C_{\max}$).

If Eq. (35) had been well posed, the solution would have been

$$\mathbf{X}^{k+1} = \mathbf{X}^k (1 + \log(\mathbf{F}^m/\mathbf{F})\mathbf{C}^{-1}), \tag{37}$$

where the superscript -1 denotes the pseudoinversion (coincides with the usual inversion if the matrix were square and corresponds to the least-squares solution otherwise).

However, Eq. (35) is ill-posed; when the number of layers N increases, some eigenvalues of $\mathbf{C}$ vanish. It leads to uncontrolled increase of error. Therefore, regularization is needed. There are various kinds of regularization, depending on the type of *a priori* information. We use the singular value decomposition as a regularization method. According to this method, instead of adding some quantity (Lagrange multiplier) to the eigenvalues of the ill-posed matrix, the eigenvalues that are less than some predefined level are just omitted. This level should be estimated from physical criteria. The error in $\mathbf{X}$ can be estimated as (see Appendix A)

$$\mathrm{err}_X = \frac{1}{\lambda_{\min}\sqrt{2N+1}} \mathrm{err}_F, \tag{38}$$

where $\lambda_{\min}$ is the minimum eigenvalue. So, the decomposition critical value λ_{cr} should be estimated as

$$\lambda_{cr} = \frac{1}{\sqrt{2N+1}}, \tag{39}$$

and all values smaller than λ_{cr} should be thrown out. In this case the error of retrieval will be approximately the same as the error of measurement. This regularization procedure based on the singular value decomposition is not mandatory, as any expedient type of regularization can be used.

6. Simulation Results

To validate our algorithm we use the closed scheme of a computer experiment. We take some profiles of cloud characteristics that are considered true ones. Lidar returns with two FOVs from this cloud are simulated as it is described in Section 2 with shot noise added. We will refer to these lidar returns as "measured" signals. The maximal signal value is normalized to 10^4 photocounts. The retrieved profiles are then found through the iteration scheme, Eq. (37), the iterations being stopped when the difference (Euclid distance) between solutions is less than the error, Eq. (38). Usually, it takes a few (less than ten) iterations.

Figures 4–7 present the true and retrieved profiles. The signals (measured and computed with retrieved profiles) are given in the top plot, while the middle and bottom plots depict the scattering coefficients and the droplet radii (true and retrieved). Different cloud profiles and different cloud dissections into sublayers for the retrieval procedure are considered.

Figures 4 and 5 present results for a homogeneous cloud. The retrieval is performed under assumptions that the cloud is 5-layered (Fig. 4) and 20-layered (Fig. 5). The increase of retrieval errors with the number of sublayers is pronounced, particularly at large optical depths.

Figures 4 and 5 show the retrievals performed at two different altitude resolutions (the sublayer thicknesses are 60 and 15 m, respectively). The crucial point here is that the signals calculated with the

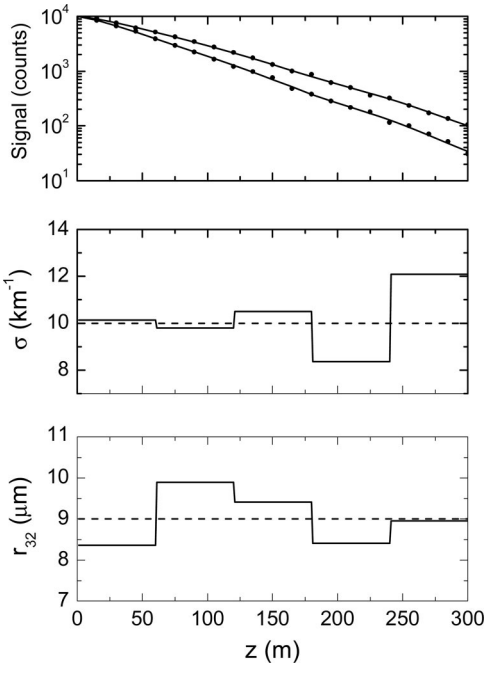

Fig. 4. Top plot—signals, measured (•) and calculated with retrieved profiles (—) for the receiver FOVs of 0.25 and 1 mrad. Middle and bottom plots—the scattering coefficient and the drop size profiles, respectively, true (dashes) and retrieved (solid) values. Receiver spatial resolution is 15 m. The true cloud is homogeneous, the retrieved cloud profile is considered as five layered.

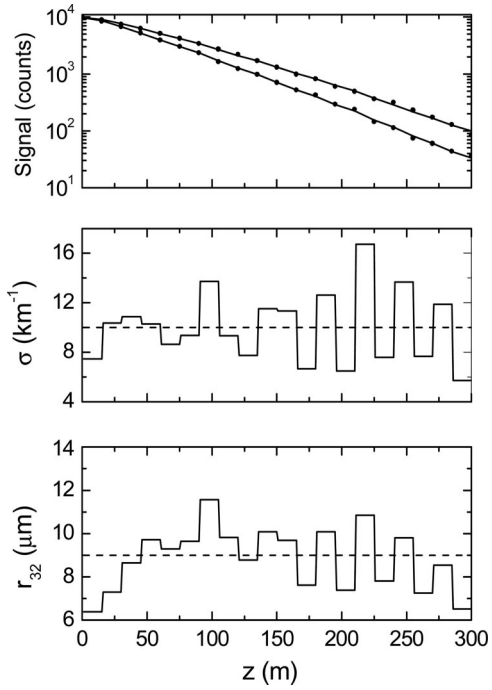

Fig. 5. Same as Fig. 4, but the retrieved cloud profile is considered as 20 layered.

retrieved profiles fit the measured signals within the accuracy of measurement. Clearly, it is pointless to retrieve the profile with a resolution of 15 m if the same signal fit is achieved with a resolution of 60 m. This fact sets the problem of the optimization of cloud dissections into sublayers to get reasonable results.

High uniform altitude resolution (low sublayer thickness) may be used for comparatively thin clouds.

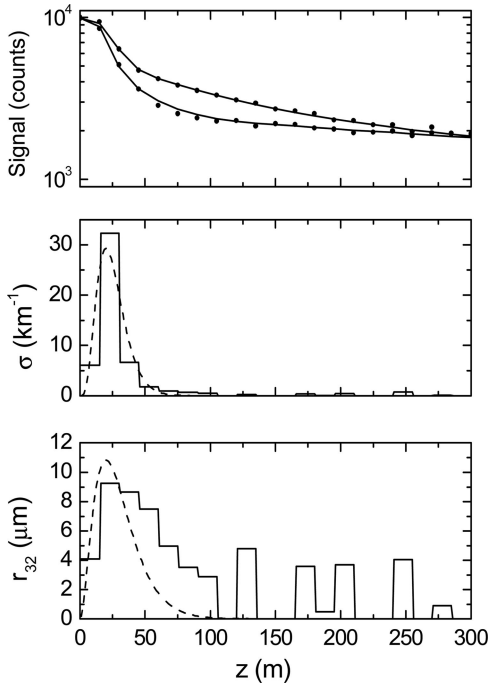

Fig. 6. Same as Fig. 5, but the true cloud is thin.

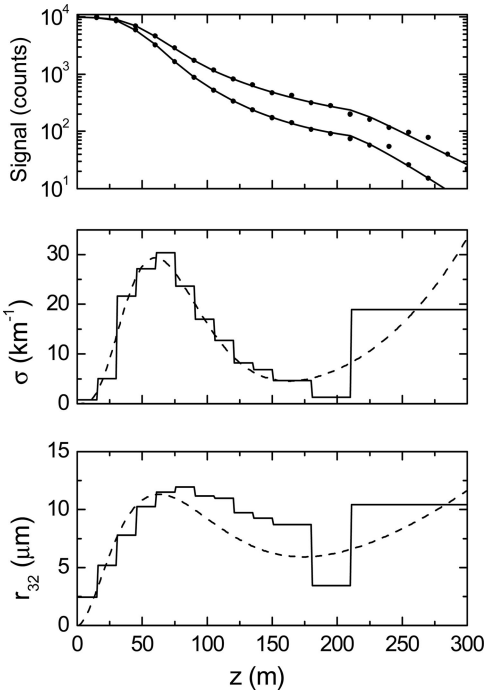

Fig. 7. Same as Fig. 5, but the true cloud is thick and has a complex profile. Retrieval is performed with variable sublayer thickness.

Such an example is presented in Fig. 6. As seen, the retrieval is good, where the cloud is dense enough (below 30 m). Above 30 m the multiple scattering is poor and the radius retrieval is inaccurate. Above 60 m the cloud is absent (the scattering is zero), so the retrieved radii values should be treated as pure noise.

This high uniform altitude resolution could not be used for thick clouds (see, e.g., Fig. 5). In this case the cloud dissection with a variable layer thickness should be recommended. In the beginning of the sounding path the signal energy is quite high, and so is the amount of photocounts. Therefore, the altitude resolution could be high enough in the near-bottom range, and vice versa for large optical depths the altitude resolution could not be high, because of the low signal-to-noise ratio.

To adjust the interval thickness as a function of z we propose the following criterion: the mean error of signal measurement err_i at each interval i, divided by the square root of the number of points in the interval n_i, should not be greater than the mean error of the signal measurement err all over the sounding range:

$$\frac{\mathrm{err}_i}{\sqrt{n_i}} \le \mathrm{err}. \tag{40}$$

(See Eqs. (A1) and (A2) for the error definition.) If the signal was independent of or slightly dependent on depth, this condition would provide the homogeneous distribution of error over the intervals. The adjustment of various sublayer thicknesses could make Eq. (35) less ill-posed, so that one would have less information lost due to regularization.

The example of retrieval with variable layer thickness is presented in Fig. 7. It is seen that the resolution is high at the cloud bottom (and corresponds to the spatial resolution of the lidar receiver) and becomes lower at high optical depths. Generally, this approach allows for good retrieval for the cloud with complex profile. Let us emphasize that the possibility to retrieve quite accurate profiles at the bottom of the cloud with good resolution from lidar data is of great importance for the synergy of lidar and radar cloud sounding.

7. Discussion

The lidar system parameters used in our simulation were chosen to be close to real Raman lidars [see, e.g., 9,10]. Because of the weakness of Raman lidar signals, Raman lidars operate in the photon counting mode and do not have high spatial resolution. The spatial resolution of Raman lidar determines the minimal sublayer thickness (maximum layers number) in the retrieval procedure. As a result, only the values of cloud parameters somewhat averaged over a particular sublayer are retrieved. This is the reason why we retrieve the profile as a set of rectangular steps. Surely, one can apply a smoothing procedure (e.g., spline), however, being aware that this information is extrinsic.

The two main features of the proposed method are as follows. The greater the value of the scattering coefficient in the layer, the better the accuracy of the drop size retrieval in this layer; and the spatial resolution of the retrieval is better at the front part of the cloud than at its far end. The former is because the physical basis of drop size retrieval is multiple scattering, and the latter is due to fast lidar return attenuation with depth and thereafter vanishing of the signal-to-noise ratio. The ability to retrieve the profile at the cloud bottom with high spatial resolution can serve as a keystone in the development of new methods of lidar–radar cloud profiling.

Appendix A

We define the average relative error of $\mathbf{X}$ as

$$\mathrm{err}_X^{\,2} = \frac{\overline{\boldsymbol{\delta}\mathbf{x}\cdot\widetilde{\boldsymbol{\delta}\mathbf{x}}}}{L}, \tag{A1}$$

where $\boldsymbol{\delta}\mathbf{x}$ is the vector of relative errors of $\mathbf{X}$:

$$\delta x_i = \frac{\Delta X_i}{X_i}, \tag{A2}$$

L is its length, the sign $\sim$ denotes matrix transpose, and the sign $-$ denotes averaging over realizations. If $\boldsymbol{\delta}\mathbf{x}$ is linearly related to $\boldsymbol{\delta}\mathbf{f}$,

$$\boldsymbol{\delta}\mathbf{f} = \boldsymbol{\delta}\mathbf{x}\mathbf{C}, \tag{A3}$$

the least-squares solution is

$$\boldsymbol{\delta}\mathbf{x} = \boldsymbol{\delta}\mathbf{f}\tilde{\mathbf{C}}\left(\mathbf{C}\tilde{\mathbf{C}}\right)^{-1}. \tag{A4}$$

So for error we have

$$\mathrm{err}_X^{\,2} = \frac{1}{L}\,\overline{\boldsymbol{\delta}\mathbf{f}\tilde{\mathbf{C}}\left(\mathbf{C}\tilde{\mathbf{C}}\right)^{-2}\mathbf{C}\widetilde{\boldsymbol{\delta}\mathbf{f}}}. \tag{A5}$$

It equals

$$\mathrm{err}_X^{\,2} = \frac{1}{L}\,Sp\left(\overline{\widetilde{\boldsymbol{\delta}\mathbf{f}}\boldsymbol{\delta}\mathbf{f}}\tilde{\mathbf{C}}\left(\mathbf{C}\tilde{\mathbf{C}}\right)^{-2}\mathbf{C}\right), \tag{A6}$$

where Sp is the matrix spur.

The correlation matrix $\overline{\widetilde{\boldsymbol{\delta}\mathbf{f}}\boldsymbol{\delta}\mathbf{f}}$ has components $\delta f_i \delta f_k$, so, as the signal values at different points do not correlate, the nondiagonal elements of matrix $\overline{\widetilde{\boldsymbol{\delta}\mathbf{f}}\boldsymbol{\delta}\mathbf{f}}$ are equal to zero. Its diagonal elements are equal to the average relative error of signal measurement

$$\overline{\delta f_k^{\,2}} = \mathrm{err}_F^{\,2}. \tag{A7}$$

Equation (A7) is true if the signal error is uniform. This is surely not the case of lidar return, however, we use this assumption for a rough estimation of the error.

It follows from Eqs. (A6) and (A7) that

$$\mathrm{err}_X^{\,2} = \frac{\mathrm{err}_F^{\,2}}{L}\,Sp\left(\left(\mathbf{C}\tilde{\mathbf{C}}\right)^{-1}\right) = \frac{\mathrm{err}_F^{\,2}}{L}\sum_k \frac{1}{\lambda_k^{\,2}}, \tag{A8}$$

where $\lambda_k^{\,2}$ is the eigenvalue of the matrix $\mathbf{C}\tilde{\mathbf{C}}$ (λ_k is the pseudoeigenvalue of the matrix C). Because the eigenvalues $\lambda_k^{\,2}$ differ strongly, the sum in Eq. (A8) can be estimated as

$$\sum_k \frac{1}{\lambda_k^{\,2}} \approx \frac{1}{\lambda_{\min}^{\,2}}. \tag{A9}$$

Estimation of the $\mathbf{X}$ error follows straightforwardly from Eqs. (A8) and (A9):

$$\mathrm{err}_X = \frac{\mathrm{err}_F}{\lambda_{\min}\sqrt{L}}. \tag{A10}$$

The authors are grateful to Ulla Wandinger for the valuable discussions. This work was partially supported by INTAS (05-1000008-8024), the Belarusian Republican Foundation for Fundamental Research (F07MS-026), and the Saxon State Ministry of Science and the Fine Arts.

References

1. A. Arking, "The radiative effects of clouds and their impact on climate," Bull. Am. Meteorol. Soc. **72,** 795–813 (1991).
2. *Climate Change Science: An Analysis of Some Key Questions* (National Academy Press, 2001) (http://books.nap.edu/).
3. K. Sassen, "Polarization lidar for identifying indirect aerosol effects on clouds," in *Proceedings of the 6th International Symposium on Tropospheric Profiling: Needs and Technologies*

(ISTP, 2003), U. Wandinger, R. Engelmann, and K. Schmieder, eds. (Institute for Tropospheric Research, 2003), pp. 184–186.
4. D. P. Donovan and A. C. A. P. van Lammeren, "Cloud effective particle size and water content profile retrievals using combined lidar and radar observation. Part 1," J. Geophys. Res. **106,** 27425–27448 (2001).
5. H. Sauvageot and J. Omar, "Radar reflectivity of cumulus clouds," J. Geophys. Res. C: Oceans Atmos. **4,** 264–272 (1987).
6. I. R. Paluch, C. A. Knight, and L. J. Miller, "Cloud liquid water and radar reflectivity of nonprecipitating cumulus clouds," J. Atmos. Sci. **53,** 1587–1603 (1996).
7. E. J. O'Connor, A. J. Illingworth, and R. J. Hogan, "Remote sensing of stratocumulus using radar/lidar synergy," in *Proceedings of the 6th International Symposium on Tropospheric Profiling: Needs and Technologies (ISTP, 2003),* U. Wandinger, R. Engelmann, and K. Schmieder, eds. (Institute for Tropospheric Research, 2003), pp. 178–180.
8. A. A. Kokhanovskii and E. P. Zege, "Parametrization of local optical characteristics of cloudy media," Izv. Acad. Sci. USSR Atmos. Oceanic Phys. **33,** 190–198 (1997).
9. A. Ansmann, M. Reibesell, and C. Weitkamp, "Measurement of atmospheric aerosol extinction profiles with Raman lidar," Opt. Lett. **15,** 746–748 (1990).
10. J. Reichardt, U. Wandinger, M. Serwazi, and C. Weitkamp, "Combined Raman lidar for aerosol, ozone, and moisture measurements," Opt. Eng. **35,** 1457–1465 (1996).
11. L. Bissonnette and D. Hutt, "Multiple scattering lidar," Appl. Opt. **29,** 5045–5046 (1990).
12. G. Roy, L. Bissonnette, C. Bastille, and G. Vallee, "Estimation of cloud droplet-size density distribution from multiple-field-of-view lidar returns," Opt. Eng. **36,** 3404–3415 (1997).
13. L. R. Bissonnette, G. Roy, and N. Roy, "Multiple-scattering-based lidar retrieval: method and results of cloud probings," Appl. Opt. **44,** 5565–5581 (2005).
14. L. R. Bissonnette, G. Roy, and G. Tremblay, "Lidar-based characterization of the geometry and structure of water clouds," J. Geophys. Res. C: Oceans Atmos. **24,** 1364–1376 (2007).
15. I. Polonskii, E. Zege, and I. L. Katsev, "Lidar sounding of warm clouds and determination of their microstructure parameters," Izv. Acad. Sci. USSR Atmos. Oceanic Phys. **37,** 624–632 (2001).
16. I. Veselovskii, M. Korenskii, V. Griaznov, D. N. Whiteman, M. McGill, G. Roy, and L. Bissonnette, "Information content of data measured with a multiple-field-of-view lidar," Appl. Opt. **45,** 6839–6848 (2006).
17. A. Malinka and E. Zege, "Using multiple scattering in Raman lidar sounding of warm clouds," in *Proceedings of the 6th International Symposium on Tropospheric Profiling: Needs and Technologies (ISTP, 2003),* U. Wandinger, R. Engelmann, and K. Schmieder, eds. (Institute for Tropospheric Research, 2003), pp. 297–299.
18. A. Malinka, "Raman lidar remote sensing of geophysical media," in *Light Scattering Reviews 2: Remote sensing and inverse problems,* A. Kokhanovsky, ed. (Springer, 2007), pp. 125–155.
19. A. V. Malinka and E. P. Zege, "Analytical modeling of Raman lidar return, including multiple scattering," Appl. Opt. **42,** 1075–1081 (2003).
20. E. Zege, A. Ivanov, and I. Katsev, *Image Transfer Through a Scattering Medium* (Springer-Verlag, 1991).
21. A. Kokhanovsky, *Optics of Light Scattering Media: Problems and Solutions* (Springer-Verlag, 2001).
22. H. C. van de Hulst, *Light Scattering by Small Particles* (Wiley, 1957).
23. D. Deirmendjian, *Electromagnetic Scattering on Spherical Polydispersions* (Elsevier, 1969).
24. W. H. Press, S. A. Teukolsky, W. T. Vetterling, and B. P. Flannery, *Numerical Recipes in C: The Art of Scientific Computing.* 2nd ed. (Cambridge U. Press, 1992).